Journal Pre-proofs

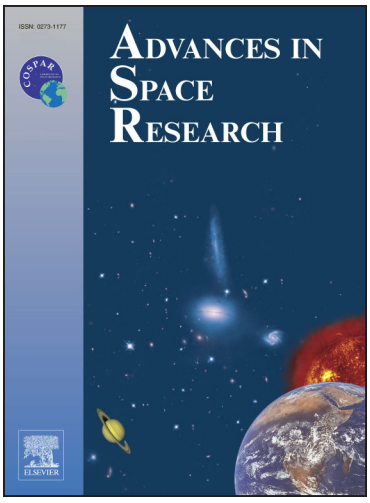

SuperTIGER instrument abundances of galactic cosmic rays for the charge interval 41Z56

Nathan Elliot Walsh, Yosui Akaike, Walter Robert Binns, Richard G. Bose, Terri J. Brandt, Dana L. Braun, Nicholas W. Cannady, Paul F. Dowkontt, Thomas Hams, Martin H. Israel, John F. Krizmanic, Allan W. Labrador, Richard A. Mewaldt, John W. Mitchell, Ryan P. Murphy, Georgia A. de Nolfo, Scott Nutter, Martin A. Olevitch, Brian. F. Rauch, Kenichi Sakai, Makoto Sasaki, Garry E. Simburger, Ed C. Stone, Teresa Tatoli, John Ennis Ward, Mark E. Wiedenbeck, Wolfgang V. Zober

PII: S0273-1177(22)00340-4
DOI: https://doi.org/10.1016/j.asr.2022.04.063
Reference: JASR 15897

To appear in: *Advances in Space Research*

Received Date: 1 November 2021
Revised Date: 22 March 2022
Accepted Date: 26 April 2022

Please cite this article as: Walsh, N.E., Akaike, Y., Binns, W.R., Bose, R.G., Brandt, T.J., Braun, D.L., Cannady, N.W., Dowkontt, P.F., Hams, T., Israel, M.H., Krizmanic, J.F., Labrador, A.W., Mewaldt, R.A., Mitchell, J.W., Murphy, R.P., de Nolfo, G.A., Nutter, S., Olevitch, M.A., Rauch, n.F., Sakai, K., Sasaki, M., Simburger, G.E., Stone, E.C., Tatoli, T., Ward, J.E., Wiedenbeck, M.E., Zober, W.V., SuperTIGER instrument abundances of galactic cosmic rays for the charge interval 41Z56 , *Advances in Space Research* (2022), doi: https://doi.org/10.1016/j.asr.2022.04.063

This is a PDF file of an article that has undergone enhancements after acceptance, such as the addition of a cover page and metadata, and formatting for readability, but it is not yet the definitive version of record. This version will undergo additional copyediting, typesetting and review before it is published in its final form, but we are providing this version to give early visibility of the article. Please note that, during the production process, errors may be discovered which could affect the content, and all legal disclaimers that apply to the journal pertain.

© 2022 COSPAR. Published by Elsevier B.V. All rights reserved.

Journal Pre-proofs

Nathan Elliot Walsh[a], Yosui Akaike[b], Walter Robert Binns[a], Richard G. Bose[a], Terri J. Brandt[c], Dana L. Braun[a], Nicholas W. Cannady[d,e,f], Paul F. Dowkontt[a], Thomas Hams[d,e,f], Martin H. Israel[a], John F. Krizmanic[d,e,f], Allan W. Labrador[j], Richard A. Mewaldt[j], John W. Mitchell[e], Ryan P. Murphy[a], Georgia A. de Nolfo[g], Scott Nutter[l], Martin A. Olevitch[a], Brian. F. Rauch[a], Kenichi Sakai[d,e,f], Makoto Sasaki[e,f,h], Garry E. Simburger[a], Ed C. Stone[j], Teresa Tatoli[g,i], John Ennis Ward[a], Mark E. Wiedenbeck[j,k], Wolfgang V. Zober[a]

[a]Department of Physics and McDonnell Center for the Space Sciences, Washington University, St. Louis, MO 63130-4899, USA
[b]Waseda Research Institute for Science and Engineering, Waseda University, Tokyo 162-0044, Japan
[c]NASA Goddard Space Flight Center, Greenbelt, MD 20771, USA
[d]Center for Space Sciences and Technology, University of Maryland Baltimore County, Baltimore, MD 21250, USA
[e]Center for Research and Exploration in Space Sciences and Technology, NASA/GSFC, Greenbelt, MD 20771, USA
[f]Astroparticle Physics Laboratory, NASA/GSFC, Greenbelt, MD 20771, USA
[g]Heliospheric Physics Laboratory, NASA/GSFC, Greenbelt, MD 20771, USA
[h]Department of Astronomy, University of Maryland, College Park, MD 20742, USA
[i]Department of Physics, Catholic University of America, Washington, DC 20064, USA
[j]California Institute of Technology, Pasadena, CA 91125, USA
[k]Jet Propulsion Laboratory, Pasadena, CA 91109, USA
[l]Northern Kentucky University, Newport, KY 41099, USA

Journal Pre-proofs

Manuscript Click here to view linked References

Journal Pre-proofs

Available online at www.sciencedirect.com

ScienceDirect

Advances in Space Research xx (2022) xxx-xxx

ADVANCES IN SPACE RESEARCH (a COSPAR publication)

www.elsevier.com/locate/asr

SuperTIGER instrument abundances of galactic cosmic rays for the charge interval $41 \leq Z \leq 56$

N. E. Walsh[a,*], Y. Akaike[b], W. R. Binns[a], R. G. Bose[a], T. J. Brandt[c], D. L. Braun[a], N. W. Cannady[d,e,f], P. F. Dowkontt[a], T. Hams[d,e,f], M. H. Israel[a], J. F. Krizmanic[d,e,f], A. W. Labrador[j], R. A. Mewaldt[j], J. W. Mitchell[e], R. P. Murphy[a], G. A. de Nolfo[g], S. Nutter[l], M. A. Olevitch[a], B. F. Rauch[a], K. Sakai[d,e,f], M. Sasaki[e,f,h], G. E. Simburger[a], E. C. Stone[j], T. Tatoli[g,i], J. E. Ward[a], M. E. Wiedenbeck[j,k], W. V. Zober[a]

[a]*Department of Physics and McDonnell Center for the Space Sciences, Washington University, St. Louis, MO 63130-4899, USA*
[b]*Waseda Research Institute for Science and Engineering, Waseda University, Tokyo 162-0044, Japan*
[c]*NASA Goddard Space Flight Center, Greenbelt, MD 20771, USA*
[d]*Center for Space Sciences and Technology, University of Maryland Baltimore County, Baltimore, MD 21250, USA*
[e]*Center for Research and Exploration in Space Sciences and Technology, NASA/GSFC, Greenbelt, MD 20771, USA*
[f]*Astroparticle Physics Laboratory, NASA/GSFC, Greenbelt, MD 20771, USA*
[g]*Heliospheric Physics Laboratory, NASA/GSFC, Greenbelt, MD 20771, USA*
[h]*Department of Astronomy, University of Maryland, College Park, MD 20742, USA*
[i]*Department of Physics, Catholic University of America, Washington, DC 20064, USA*
[j]*California Institute of Technology, Pasadena, CA 91125, USA*
[k]*Jet Propulsion Laboratory, Pasadena, CA 91109, USA*
[l]*Northern Kentucky University, Newport, KY 41099, USA*

Received 31 October 2021; Received in final form XX October 2021; Accepted XX October 2021;
Available online XX October 2021

Abstract

We report preliminary elemental abundance results from the 55-day long-duration-balloon flight of SuperTIGER (Super Trans-Iron Galactic Element Recorder) during the 2012-2013 austral summer. SuperTIGER measured the relative abundances of Galactic cosmic-ray (GCR) nuclei with high statistical precision and well resolved individual element peaks from $_{10}$Ne to $_{40}$Zr. SuperTIGER also made exploratory measurements of the relative abundances up to $_{56}$Ba. Although the statistics are low for elements heavier than $_{40}$Zr, we present, for the first time, relative abundance measurements of charges $Z = 41 - 56$ with individual element resolution. GCR measurements up to $_{40}$Zr support a source acceleration model where supernovae in OB associations preferentially accelerate refractory elements that are more readily embedded in interstellar dust grains than volatiles. In addition, injection into the GCR for both refractory and volatile elements appears to follow a charge dependence consistent with their grain sputtering cross sections. By extending the GCR measurement range past $_{40}$Zr, we can begin to further constrain these models.
© 2022 COSPAR. Published by Elsevier Ltd All rights reserved.

Keywords: galactic cosmic rays; supernova; binary neutron star merger; long-duration balloon; Antarctica

*Corresponding author: Tel.: +1-314-471-7800;
Email address: newalsh@wustl.edu (N. E. Walsh)

https://dx.doi.org/10.1016/j.jasr.xxxx.xx.xxx
0273-1177/© 2022 COSPAR. Published by Elsevier Ltd All rights reserved.

Journal Pre-proofs

1. Introduction

The study of the Galactic Cosmic-Ray Source (GCRS) has been pursued for over half a century and still remains an open question in astrophysics. Measurements of GCR elemental and isotopic abundances are made to understand the GCRS composition in order to constrain the theories of GCR origin. The current explanation is that the majority of GCR originate within OB associations, where many young, massive stars of spectral type O and B reside, leading to a high rate of supernovae (SNe) that occur in close proximity to one another (Reeves (1973), and later Higdon & Lingenfelter (2005) and references therein). These SNe produce shock waves that sweep up and accelerate to GCR energies the surrounding interstellar medium (ISM) including some massive star material (MSM) produced by stellar winds and previous SN explosions within the OB association.

The volatility model of GCR acceleration was proposed by Epstein (1980) in which it was argued that elements likely to form interstellar dust grains (refractory elements; those with condensation temperatures $T_c > 1250$ K as in Ellison et al. (1997)) should be preferentially accelerated over those that exist primarily as interstellar gasses (volatile elements; $T_c < 1250$ K). Because it involves magnetic reflection, diffuse shock acceleration is more efficient for particles with high rigidity. The higher mass-to-charge ratio of interstellar dust grains gives them a higher rigidity than the individual nuclei in interstellar gasses, allowing them to be accelerated more readily. This theory suggests that the refractories will be enhanced relative to the volatiles in GCR abundances measurements and that the volatiles will follow a mass dependent enhancement trend. As they are accelerated within grains, the refractory abundances should not see such a mass dependence. More recently, however, Lingenfelter (2019) proposed that the apparent atomic mass dependence seen in the refractory abundance enhancement by TIGER (Rauch et al., 2009) and SuperTIGER (Murphy et al., 2016) can actually be explained by the atomic charge dependent sputtering of refractory elements from the surfaces of the grains they condense into. The theory assumes that *all* GCR are accelerated within dust grains and that the refractory enhancement over the volatiles is a result of the increased likelihood that refractories will be embedded in grains. If both refractories and volatiles are accelerated within grains, the previously seen mass dependence of both GCR types is explained instead by a sputtering probability that comes from the charge dependent ($\propto Z^{2/3}$) cross sections of the grain surface elements of charge Z with ambient H and He. This theory is demonstrated in Figure 1 from Lingenfelter (2019).

SuperTIGER (Murphy et al., 2016) made the first GCR measurements of all the elements in the atomic charge range $30 \leq Z \leq 40$ with individual element resolution. As described in this paper, we have extended the SuperTIGER analysis and report the first individual element GCR measurements of the $41 \leq Z \leq 56$ range. We provide these abundances as they are measured within the SuperTIGER instrument. A series of corrections are required to account for changes in flux caused by nuclear interactions and energy losses that occur within the instrument, atmosphere and interstellar medium. These corrections are required to determine the GCR elemental abundances as they are when accelerated from the GCRS and are yet to be finalized and are not reported here.

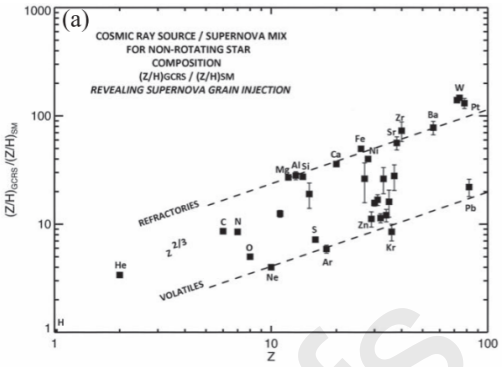

Fig. 1: GCRS abundances for: Engelmann et al. 1990 & Cummings et al. 2016, $1 \leq Z \leq 28$; Rauch et al. 2009 & Murphy et al. 2016, $26 \leq Z \leq 40$; Binns et al. 1989, $40 \leq Z \leq 70$; Donnelly et al. 2012, $Z > 70$, plotted relative to a GCRS mixture of 20% MSM (Woosley and Heger 2007) and 80% SS (Lodders 2003). Normalized to an $_1$H ratio of 1. Figure from Lingenfelter (2019).

2. The SuperTIGER Instrument

The SuperTIGER instrument is optimized to measure the relative abundances of heavy and ultra-heavy Galactic cosmic-ray nuclei and has made single element measurements in the charge range $10 \leq Z \leq 40$ (Neon to Zirconium) with good statistics and individual-element charge resolution (Murphy et al., 2016). In addition, it is capable of making exploratory measurements up to $Z = 60$ (Neodymium). During the 2012-13 Austral summer, SuperTIGER flew from Williams Field Antarctica on a long duration balloon for 55 days, maintaining and average altitude of 125,000 ft. During its flight, SuperTIGER recorded over 5 million cosmic-ray iron events, $\sim$ 4500 events with $30 \leq Z \leq 40$, and 212 events with $41 \leq Z \leq 56$.

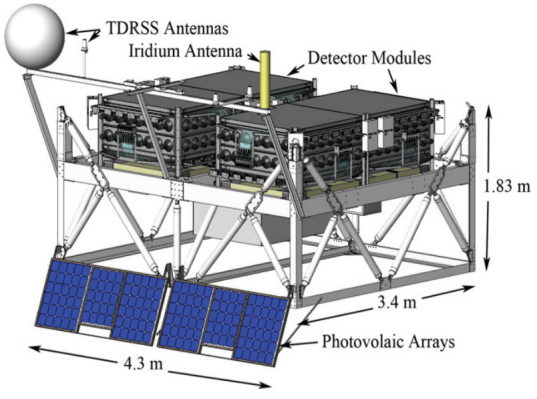

Fig. 2: Technical model of the SuperTIGER payload with both instrument modules mounted in the gondola. Each module operates independently of the other.

The SuperTIGER instrument is composed of two nearly identical modules (Figure 2). Half of each module resembles its predecessor, the TIGER instrument (Rauch et al., 2009), making it roughly equivalent to 4 TIGER instruments working to-

Journal Pre-proofs

gether. Each SuperTIGER module contains seven stacked detectors, as shown in Figure 3 (Binns et al., 2014). From top to bottom, in each module there is a plastic scintillation detector (S1) used for charge determination and as part of the trigger coincidence, a scintillating optical fiber hodoscope plane (H1) that detects the (x, y) position near the top of the instrument, a silica-aerogel Cherenkov detector (C0) and an acrylic Cherenkov detector (C1) that are both used for charge and energy determination, a second scintillation detector (S2) used for charge determination and coincidence, a second hodoscope plane (H2) that detects the (x, y) position near the bottom of the instrument, and a third scintillation detector (S3) used mostly to reject particles that interacted in the instrument, but also as a backup to S2 should it fail during flight. The signals from the S and C detectors are used in combination to measure the charge and kinetic energy of cosmic rays that are able to pass through the entire stack without interacting. The H layer position measurements are used to determine the trajectory of each cosmic ray through the instrument, allowing angle corrections and area non-uniformity corrections to be performed.

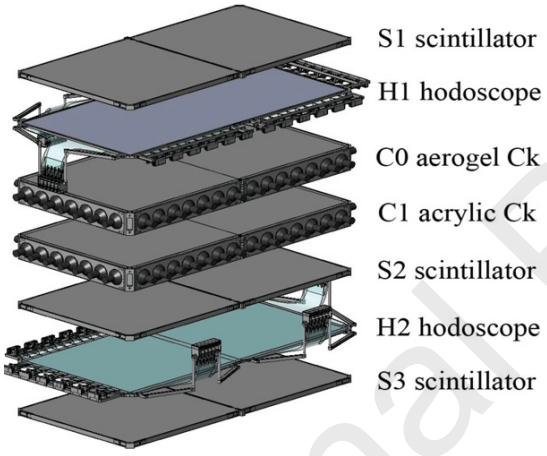

Fig. 3: One module of the SuperTIGER instrument (expanded).

Signals from the photomultiplier tubes (PMTs) in each detector are read out by custom front-end electronics (FEE) boards. The scintillator FEE boards contain fast-shaping amplifiers that enable a rough charge estimate used for establishing charge dependent triggers. For particles that are estimated to have charge $Z \gtrsim 10$, the event is recorded in full on solid state drives (SSDs) that are present on each module and buffered for telemetry in a compressed format via the Tracking and Data Relay Satellite System (TDRSS) when possible. Particles with estimated charge $Z \gtrsim 22$ are tagged as "high priority" and are telemetered ahead of other events when TDRSS bandwidth is available.

3. Charge Assignment Method

SuperTIGER is designed to measure GCR events with excellent charge resolution over a broad range ($\sim$ 320 MeV/nucleon through $\sim$ 10 GeV/nucleon) of the GCR energy spectrum. This is made possible by employing two complementary charge assignment techniques, one that resolves charges well for lower GCR energies and another that does for the higher GCR energies. These charge assignment methods are both optimized to analyze the extremely rare ultra-heavy GCR ($Z \geq 30$) whose abundances are the focus of this work. The signals from each detector layer used for charge determination in this analysis (S1, S2, C0 and C1), represent the angle and area corrected sum of the pedestal subtracted, position and gain corrected PMT signals in each detector layer. Each detector signal for a given event is then proportional to the total number of photoelectrons emitted by the charged particle when it passed through each detector. The charge dependence of the signals from the scinitllation light detectors is roughly $S \propto Z^{1.7}$ and, from the Cherenkov light detectors, it is $C \propto Z^2$.

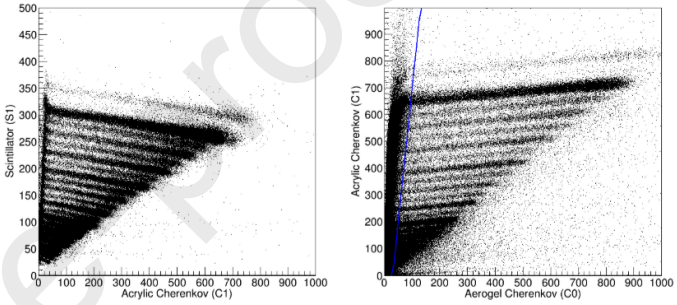

Fig. 4: A single flight day's data is plotted in C1 vs. C0 space (right panel). The data to the left of the blue line is plotted in S1 vs. C1 space (left panel).

When GCR events have energies in the instrument greater than the Cherenkov threshold of the C0 detector (2.35 GeV/nucleon for three half modules and 3.31 GeV/nucleon for the fourth) we are able to use a "Above-C0" charge assignment method that utilizes the signals from both the C0 and C1 detectors. If the GCR energy is below the C0 threshold but above the C1 threshold ($\sim$ 320 MeV/nucleon) we use a "Below-C0" charge assignment method, which uses the signals from two of three of the scintillation detectors (S1 or S2) in combination with the C1 signal. For both the Above- and Below-C0 methods, cross plots of the aforementioned signals are created, revealing well resolved charge bands that can be analyzed (Figure 4). For reference, the highest visible band is nickel ($Z = 28$). The very dense band just beneath it is iron ($Z = 26$). A cut that approximates the C0 turn-on threshold is made on the C1 vs. C0 cross plot. This cut separates the entire SuperTIGER data set into two subsets that are each compatible with either the Above- or Below-C0 methods. This is illustrated in Figure 4 where the left plot (S1 vs. C1) shows only data to the left of the blue line drawn on the right plot (C1 vs. C0). The left plot includes only the particles with energies below the C0 Cherenkov threshold and so the Below-C0 method is used on these data. The Above-C0 method, then, is used on the particles to the right of the blue line drawn in the right plot that have energies above the C0 Cherenkov threshold. Notice that the elements heavier than nickel are too scarce to form visible charge bands. In order to measure the abundances of elements heavier than nickel (and in particular the exceedingly rare $41 \leq Z \leq 56$

Journal Pre-proofs

range), we must accurately determine the charge dependence of the detector response using the visible charge bands and extrapolate this dependence into the UH range.

3.1. Above-C0 Charge Assignment

For cosmic-ray events with energies greater than the turn-on threshold of SuperTIGER's aerogel Cherenkov (C0) detector, the Above-C0 method for charge assignment is used. As shown previously (Figure 4), the Above-C0 method analyzes the well resolved charge events to the right of the cut in C1 vs. C0 space. Because one half-module of C0 has a radiator of different refractive index (n_0 = 1.025 as opposed to n_0 = 1.043), the analysis for this half-module must be done separately. Using the particle trajectories determined by the hodoscope and the known vertical distances of the C0 radiators from the hodoscope, the location that the particle passed through the C0 radiator can be determined. The Above-C0 data subset is separated into four additional subsets based on which half-module the particles traversed.

In the C1 vs. C0 cross plot shown in Figure 4, charge bands form that appear to follow regularly spaced nearly straight lines. In fact, it can be shown that, given a sample of GCR events each yielding two pure Cherenkov signals in different radiating materials, these events should land on a family of parallel lines (or bands) that are separated based on charge ($\propto Z^2$). In short, only one equation that describes a single charge band is needed to determine the equations that describe all other charge bands formed from signals made by the same two Cherenkov detectors. To characterize this effect we examine the band for iron nuclei, as it is the most populated sample near to the UH region and thus gives the best extrapolation possible to the very high charges. We scale the signal space to the iron band and find that its shape is well fitted by a quadratic function. The charge bands are not perfectly straight due to small contributions from scintillation in detector materials and Cherenkov emission from delta rays in addition to the Cherenkov emission from the cosmic ray. The quadratic fit accounts for these small contributions. Given the functional form for the bands and the values for C0 and C1 in this scaled signal space, we can calculate the charge of all incident particles above the C0 threshold.

To illustrate the procedure, for each of 30 angle bins, we fill a cross plot with $\sqrt{C1}/26$ vs. $\sqrt{C0}/26$ points to create a space that is scaled to iron (Z = 26). The square root of each signal is used because the Cherenkov light collected is proportional to Z^2 and so the square root of the signal is proportional to the charge. The iron band is then isolated and separated into 50 $\sqrt{C0}/26$ bins that span the region between the Above-C0 cut and the end of the iron band. Each bin is projected onto the $\sqrt{C1}/26$ axis and the resulting peak is fit with a Gaussian function to find the mean $\sqrt{C1}/26$ value in each bin. The average $\sqrt{C0}/26$ value is calculated in each bin and the set of 50 ($\sqrt{C0}/26$, $\sqrt{C1}/26$) points are fit with a second order polynomial function as in Figure 5.

The iron band is fit as described above for each half-module within every angle bin. Note that the lower C0 index half-module has a flatter band structure than the other half-modules.

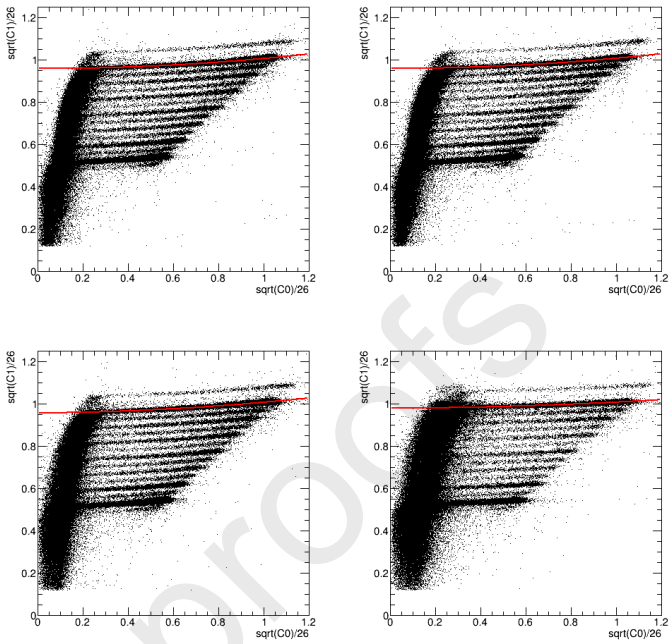

Fig. 5: Quadratic fits to the Above-C0, C1 vs. C0 iron band for each half-module in module 1 (top panels) and module 2 (bottom panels).

This is due to the fact that the particles that turn on this C0 detector half-module must have velocities of at least β=1/1.025 as opposed to β=1/1.043 in the other half-modules. The range of velocities between β=1/1.025 and β=1 is smaller than between β=1/1.043 and β=1 and so, for a given charge, the range of C1(β) values that be achieved in the first case is smaller than the later, giving a flatter spectrum over the signal space of the C0 detector.

Once the normalized iron band fitting is complete for each half-module over all angle bins, the parameters of the second order polynomial fits are used to determine a charge for the C0 and C1 signal pairing of each event in the Above-C0 data set.

3.2. Below-C0 Charge Assignment

For cosmic-ray events with energies less than the turn-on threshold of SuperTIGER's aerogel Cherenkov (C0) detectors, the Below-C0 method for charge assignment is used. As described before (Figure 4), the Below-C0 method analyzes the unresolved charge events to the left of the cut in C1 vs. C0 space. The events to the left of this cut are in fact well resolved in the S1 vs. C1 and S2 vs. C1 spaces used in the Below-C0 method. The weighted average of the charges derived by the two signal combinations (S1 or S2 with C1) yields the final Below-C0 charge assignment.

The light emitted by a scintillating material is a portion of the energy deposited dE/dx by a charged particle traversing the radiating material. This dE/dx is described by the Bethe-Bloch equation and has a simple dependence on the charge of the traveling particle (Z^2), but the kinetic energy dependence of the deposited energy is much more complicated. In order to

determine the charge dependence of the light emitted, the energy dependence must be decoupled. In addition, the saturation of the emission sites in the scintillator, when large energy deposits are made in a small region, will decrease the expected light yield dL/dx and cause the charge dependence of the measured signal to deviate from the Bethe-Bloch equation. This saturation effect is itself charge dependent, and so it is necessary to model $dL/dx(Z)$ in order to extract the charge of events. In other words, in the Below-C0 method, the fit to a single charge band no longer describes the shape and separation of the rest of the bands as it could in the Above-C0 method, where the known Z^2 dependent separation of the bands is reliable. In order to model the Below-C0 $dL/dx(Z)$, which includes strong energy dependence and saturation effects, we must determine the band separation manually, requiring fits to be done on a series of charge bands.

Within each of 30 angle bins, we plot the scintillator signals against an energy proxy, $\xi = C1/Z^2 \approx C1/S^{2/1.7}$, and divide the charge bands into 50 ξ bins that each contains an equal number of iron events. As stated above, for the Above-C0 method, it was sufficient to fit only one charge band to assign charge to the entire Above-C0 data set because the C1 vs. C0 band separation is a simple function of Z. For the Below-C0 method, in order to properly account for the charge dependent effects of scintillator saturation, we instead fit each even-charge band in S vs. ξ space, so that we may model the more complicated charge dependence of the band separation.

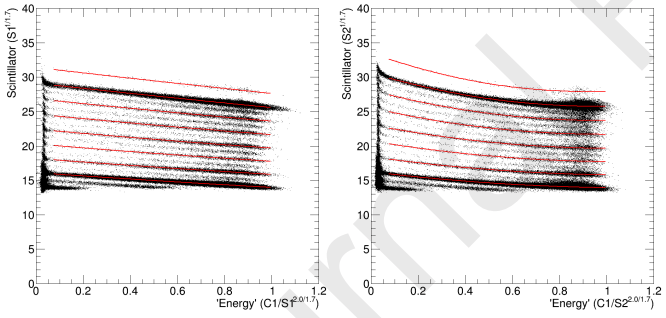

Fig. 6: Quadratic fits to the Below-C0, S vs. ξ charge bands (even charges only). The pronounced curve of the S2 vs. ξ charge bands (right) is due to energy losses sustained before cosmic rays reach the S2 detector near the middle of the detector stack. This effect is not visible for the S1 vs. ξ charge bands (left) because the S1 detector is on the very top of the detector stack.

With the shape to each well resolved even-charge band determined for every angle bin, we are able to model the charge band separation such that we can assign charge to particles far above these bands, where statistics are very low. Within each ξ bin, we fit a simplified ($d\beta/dx = 0$) saturation model to S vs. Z points (Figure 7) that are determined by the even-charge band spacing in each angle-ξ bin. The simplified Tarle et al. (1979) model used takes the form

$$S = AZ^2 + \frac{BZ^2}{1 + CZ^2}, \quad (1)$$

where S is the scintillator signal, Z is the charge of the incident particle and A, B and C are fit parameters. The parameters of the simplified Tarle model fits are saved for every angle-ξ bin combination and used to create a charge surface over angle-ξ space using bilinear interpolation. This charge surface is used to assign charge to particles with any angle-ξ combination. This process is done for both S1 and S2, resulting in two charge assignments for each event in the Below-C0 data.

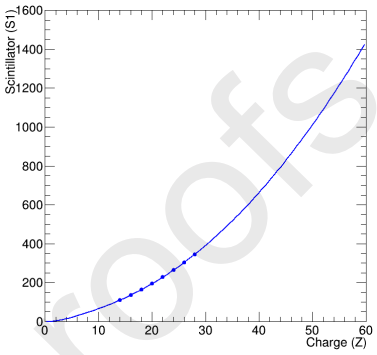

Fig. 7: The simplified Tarle (blue) saturation model fit to S1 vs. Z points for a sample angle-ξ bin combination.

3.3. Measured Instrument Abundances

To obtain a final SuperTIGER instrument-level charge histogram, we combine the three charge histograms made using the Above- and Below-C0 charge assignment methods. While the charge assignment process described above yields well resolved histograms, these three histograms are slightly misaligned due to residual effects not captured by the correction process. To account for this, each even charge peak with $Z \leq 40$ is fit with a Gaussian function and the peak means are extracted and plotted against their expected integer charges. These plots are fit with linear functions that are inverted in a follow-up charge assignment iteration to correct the charge assigned to each particle, resulting in charge histograms with peaks aligned to the integers. Table 1 shows the magnitude (in c.u.) of the shift required to align charges $Z = 30, 40$ and 56, given parameters determined for each charge assignment method.

Z	Above-C0	Below-C0 (S1)	Below-C0 (S2)
30	0.02	0.01	-0.07
40	0.17	0.20	0.16
56	0.42	0.49	0.52

Table 1: Degree of charge shift (in c.u.) required to align representative charge peaks $Z = 30, 40$ and 56.

To combine the two charge assignments performed on the Below-C0 data, we average the charges determined by both S1 and S2 with C1 and fill a "combined" Below-C0 histogram with the resulting $(Z_{S1} + Z_{S2})/2$ values. Doing this improves the Below-C0 charge resolution while conserving the number of particles treated by the Below-C0 method. The Above- and Below-C0 methods each treat a separate data set, divided by the C0 Cherenkov threshold energy. These are independent data, so

Journal Pre-proofs

Journal Pre-proofs

the final histograms from each method are simply added to obtain a combined Above- and Below-C0 charge histogram.

In order to derive the instrument level elemental abundances, the combined charge histogram resulting from the Above- and Below-C0 methods is fit with a maximum likelihood, multi-peak Gaussian function. The function is composed of 41 Gaussian functions, which each correspond to a charge peak in the range $16 \leq Z \leq 56$. The first peak position (at $Z = 16$) and the peak separation are allowed to vary and the sigma of the Gaussian peaks is assumed to vary linearly with Z. The linearity of the peak positions and sigmas, along with the final peak amplitudes, are determined by a three-stage fitting process. First, all peak positions, sigmas and amplitudes are allowed to vary freely. The sigmas of all even-charge peaks are plotted against charge and fit with a line. The sigma linearity parameters are fed into the second fitting stage, where the peak positions and amplitudes vary freely. The even-charge peak positions obtained in this second stage are plotted against charge and fit with a line. This line determines the position of the first peak ($Z = 16$) and the peak separation. Finally, with the linearity of the peak positions and sigmas determined, the fit is performed a third time where only the peak amplitudes vary.

This fitting process yields a first peak position at $Z = 16.0070$ and a peak separation of 1.00005 charge units (c.u.). The sigma values determined for peaks $Z = 16$, $Z = 26$ and $Z = 56$ are 0.179, 0.185 and 0.203 c.u., respectively. The fit result is shown in Figures 8 and 9. At last, the elemental abundances, as measured within the SuperTIGER instrument, are determined by the area of each Gaussian peak. These abundances are listed in Table 3 along with peak fit errors, determined by the error on the area of each charge peak, and statistical errors, calculated as in Gehrels (1986). As a consistency check, the abundances determined by the fit for $40 \leq Z \leq 56$ are compared with the integrated histogram counts for each element in this range. For each Z, the histogram counts are summed between $Z \pm 0.5$ c.u. The comparison is shown in Table 2. The fit determined abundances are very consistent with the integrated histogram counts for each element, with the sum of all $40 \leq Z \leq 56$ abundances over-counting the integrated histogram by only 1.1 particles.

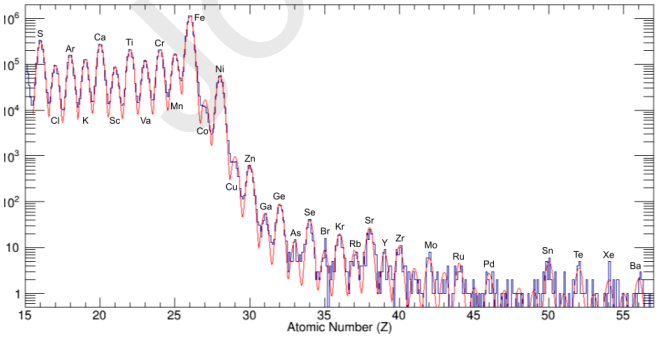

Fig. 8: The entire SuperTIGER measured charge range, $16 \leq Z \leq 56$. The charge peaks are fit with a multi-peak Gaussian function from which the elemental abundances are extracted.

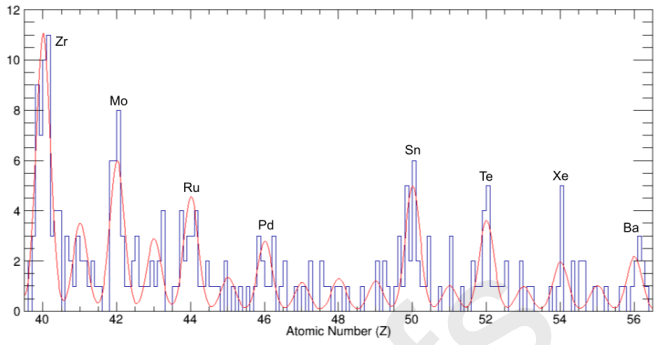

Fig. 9: SuperTIGER's newly measured charge range, $41 \leq Z \leq 56$, with multi-peak Gaussian fit result. A linear scale is used for this low statistics region.

Z	N_{INST}	N_{HIST}
40	53.6	53
41	17.0	17
42	29.2	28
43	14.1	15
44	22.4	22
45	6.6	7
46	13.7	13
47	5.7	6
48	6.5	7
49	6.0	6
50	24.9	25
51	5.1	5
52	18.1	17
53	4.9	6
54	9.9	9
55	5.2	6
56	11.1	11
SUM	254.1	253

Table 2: Fit-determined instrument abundances for $40 \leq Z \leq 56$ compared to histogram counts within $Z \pm 0.5$ c.u. for each integer charge.

4. Conclusions

For the first time, the SuperTIGER instrument has measured GCR abundances of the atomic charge range $41 \leq Z \leq 56$ with individual element resolution. To obtain GCRS abundances, these measurements must be corrected for flux changes caused by nuclear interactions and energy losses in the instrument, atmosphere and ISM. With the necessary corrections performed, these measurements will expand upon those made by TIGER (Rauch et al., 2009) and SuperTIGER (Murphy et al., 2016), which both measured GCRS abundances over the $30 \leq Z \leq 40$ range. The results of Rauch et al. (2009) and Murphy et al. (2016) support the OB association origin and SN shock wave acceleration models, where refractory GCR are preferentially accelerated compared to volatiles due to their increased likelihood to embed in interstellar dust grains. Additionally, both the refractories and volatiles are seen to follow charge dependent enhancement trends that can be explained by their $\propto Z^{2/3}$ sput-

Journal Pre-proofs

tering cross sections, as proposed by Lingenfelter (2019). We aim to finalize the necessary corrections to obtain new SuperTIGER GCRS abundance measurements of the $41 \leq Z \leq 56$ range for future publication. This 16 charge unit increase in the GCRS abundance measurement range will provide a stringent test of the current GCR origin and acceleration models.

5. Acknowledgments

This research was supported by NASA under grants NNX09AC17G, NNX14AB25G, NNX15AC23G and 80NSSC20K0405, by the McDonnell Center for the Space Sciences at Washington University, and by the Peggy and Steve Fossett Foundation.

We thank the NASA Columbia Scientific Balloon Facility, the NASA Balloon Program Office, and the NSF United States Antarctic Program for the excellent and highly professional efforts that resulted in two successful long-duration balloon flights for SuperTIGER.

References

Binns, W. R., Bose, R. G., Braun, D. L., Brandt, T. J., Daniels, W. M., Dowkontt, P. F., Fitzsimmons, S. P., Hahne, D. J., Hams, T., Israel, M. H., Klemic, J., Labrador, A. W., Link, J. T., Mewaldt, R. A., Mitchell, J. W., Moore, P., Murphy, R. P., Olevitch, M. A., Rauch, B. F., Sakai, K., Sebastian, F. S., Sasaki, M., Simburger, G. E., Stone, E. C., Waddington, C. J., Ward, J. E., & Wiedenbeck, M. E. (2014). The SuperTIGER Instrument: Measurement of Elemental Abundances of Ultra-Heavy Galactic Cosmic Rays. *The Astrophysical Journal*, *788*, 18.

Ellison, D. C., Drury, L. O., & Meyer, J.-P. (1997). Galactic Cosmic Rays from Supernova Remnants. II. Shock Acceleration of Gas and Dust. *The Astrophysical Journal*, *487*, 197–217.

Epstein, R. I. (1980). The Acceleration of Interstellar Grains and the Composition of the Cosmic Rays. *Monthly Notices of the Royal Astronomical Society*, *193*(4), 723–729.

Gehrels, N. (1986). Confidence Limits for Small Numbers of Events in Astrophysical Data. *The Astrophysical Journal*, *303*, 336–346.

Higdon, J. C., & Lingenfelter, R. E. (2005). OB Associations, Supernova-Generated Superbubbles, and the Source of Cosmic Rays. *The Astrophysical Journal*, *628*, 738–749.

Lingenfelter, R. E. (2019). The Origin of Cosmic Rays: How Their Composition Defines Their Source and Sites and the Process of Their Mixing, Injection, and Acceleration. *The Astrophysical Journal Supplement Series*, *245*, 30.

Murphy, R. P., Sasaki, M., Binns, W. R., Brandt, T. J., Hams, T., Israel, M. H., Labrador, A. W., Link, J. T., Mewaldt, R. A., Mitchell, J. W., Rauch, B. F., Sakai, K., Stone, E. C., Waddington, C. J., Walsh, N. E., Ward, J. E., & Wiedenbeck, M. E. (2016). Galactic Cosmic Rays Origins and OB Associations: Evidence from SuperTIGER Observations of Elements $_{26}$Fe through $_{40}$Zr. *The Astrophysical Journal*, *831*(2), 148.

Rauch, B. F., Link, J. T., Lodders, K., Israel, M. H., Barbier, L. M., Binns, W. R., Christian, E. R., Cummings, J. R., de Nolfo, G. A., Geier, S., Mewaldt, R. A., Mitchell, J. W., Schindler, S. M., Scott, L. M., Stone, E. C., Streitmatter, R. E., Waddington, C. J., & Wiedenbeck, M. E. (2009). Cosmic Ray Origin in OB Associations and Preferential Acceleration of Refractory Elements: Evidence from Abundances of Elements $_{26}$Fe through $_{34}$Se. *The Astrophysical Journal*, *697*(2), 2083–2088.

Reeves, H. (1973). Nucleosynthesis and the Origin of the Galactic Cosmic Rays. *Proceedings of the 13th International Cosmic Ray Conference*, *5*, 3323–3353.

Tarle, G., Ahlen, S. P., & Cartwright, B. G. (1979). Cosmic Ray Isotope Abundances from Chromium to Nickel. *The Astrophysical Journal*, *230*, 607–620.

Z	N_{INST}	±FitErr	+GehErr	−GehErr
16	1459490	1475	1209	1208
17	433580	854	659	658
18	711882	1069	845	844
19	583025	951	765	764
20	1227900	1367	1109	1108
21	410107	798	641	640
22	964170	1220	983	982
23	572988	947	758	757
24	985187	1232	994	993
25	807506	1234	900	899
26	5393040	2892	2323	2322
27	78462	372	281	280
28	267345	615	518	517
29	4608	67.1	68.9	67.9
30	3057	67.8	56.3	55.3
31	265	21.3	17.3	16.3
32	429	23.6	21.7	20.7
33	67.5	12.4	9.2	8.2
34	188	18.6	14.7	13.7
35	43.1	8.6	7.6	6.5
36	97.2	10.9	10.9	9.8
37	41.8	7.6	7.5	6.4
38	131	11.5	12.4	11.4
39	37.1	7.7	7.1	6.1
40	53.6	8.9	8.3	7.3
41	17.0	4.2	5.1	4.1
42	29.2	6.2	6.4	5.4
43	14.1	4.8	4.8	3.7
44	22.4	6.7	5.7	4.7
45	6.6	5.9	3.6	2.5
46	13.7	4.7	4.7	3.7
47	5.7	2.5	3.4	2.3
48	6.5	2.2	3.5	2.5
49	6.0	2.2	3.4	2.4
50	24.9	6.6	6.0	5.0
51	5.1	2.3	3.3	2.2
52	18.1	4.9	5.3	4.2
53	4.9	4.9	3.2	2.1
54	9.9	3.4	4.1	3.1
55	5.2	4.9	3.3	2.2
56	11.1	3.9	4.3	3.3

Table 3: Instrument level, combined Above- and Below-C0, elemental abundances for the range $16 \leq Z \leq 56$ obtained from the multi-peak Gaussian fit. Fit errors are determined by calculating the error on the area of each Gaussian peak. Statistical errors are calculated as in Gehrels (1986).

Journal Pre-proofs

Declaration of Interest Statement

SuperTIGER instrument abundances of galactic cosmic rays for the charge interval 41≤Z≤56

No authors listed on this manuscript have financial or personal relationships with other people or organizations that could inappropriately influence (bias) their work

Nathan Elliot Walsh

Journal Pre-proofs